

Enhanced removal efficiency of multicomponent VOCs over the Sn-doped Silicalite-1-supported Ru single-atom catalysts by constructing tightly coupled redox and acidic sites

Linke Wu ^{a,b}, Jiguang Deng ^{a,b,*}, Yuxi Liu ^{a,b}, Lin Jing ^{a,b}, Xiaohui Yu ^{a,b}, Jinxiong Tao ^{a,b}, Ruyi Gao ^{a,b}, Ying Feng ^{a,b}, Hongxing Dai ^{a,b,*}

^a Beijing Key Laboratory for Green Catalysis and Separation, Key Laboratory of Beijing on Regional Air Pollution Control, Key Laboratory of Advanced Functional Materials, Education Ministry of China, China

^b Laboratory of Catalysis Chemistry and Nanoscience, Department of Chemical Engineering, College of Materials Science and Engineering, Beijing University of Technology, Beijing 100124, China



ARTICLE INFO

Keywords:

Supported Ru single-atom catalyst
Tin-doped Silicalite-1
Volatile organic compound
Dichloromethane
Toluene
Catalytic oxidation

ABSTRACT

The development of cost-effective catalysts with excellent chlorine resistance and harmful by-products inhibition is important for the environmentally friendly purification of multi-component volatile organic compounds (VOCs) and chlorine-containing VOCs (CVOCs). In this work, the Sn-doped Silicalite-1-supported Ru ($\text{Ru@Silicalite-1-Sn-x}$, and x is the molar ratio of Si/Sn) samples were prepared using a hydrothermal strategy, and catalytic activities of these materials were investigated for the oxidative removal of mixed VOCs (dichloromethane (DCM) and toluene). The $\text{Ru@Silicalite-1-Sn-50}$ sample with tightly coupled redox and acidic sites exhibited high catalytic activity ($T_{90\%} = 287^\circ\text{C}$ for toluene oxidation and $T_{90\%} = 361^\circ\text{C}$ for DCM oxidation at a space velocity of 40,000 mL/(g h); specific reaction rate and turnover frequency (TOF_{Ru}) for toluene oxidation at 170°C were 9.67 $\mu\text{mol}/(\text{g}_{\text{cat}} \text{ h})$ and $0.98 \times 10^{-3} \text{ s}^{-1}$, and specific reaction rate and TOF_{Ru} for DCM oxidation at 200°C were 3.84 $\mu\text{mol}/(\text{g}_{\text{cat}} \text{ h})$ and $0.46 \times 10^{-3} \text{ s}^{-1}$, respectively), excellent catalytic stability (within 100 h of on-stream oxidation at 380°C), and effective inhibition of toxic chlorine-containing by-products formation in the oxidation of (DCM and toluene). The doping of Sn could effectively anchor the Ru atoms to result in single-atom dispersion of Ru and generate oxygen vacancies, and optimized the synergistic interaction between Lewis acid sites and Brønsted acid sites. The high concentration of oxygen vacancies and enriched Brønsted acid sites promoted the cleavage of C–Cl bonds in DCM and accelerated the desorption of Cl species as inorganic chlorine. In the meanwhile, the strong electron transfer within the Sn–O–Si bond increased the Lewis acidity, which promoted the deep oxidation of dechlorinated intermediates/other intermediates over $\text{Ru@Silicalite-1-Sn-50}$. We believe that the present work provides a feasible and promising strategy for the design of efficient catalysts for the destruction of multicomponent VOCs and CVOCs in an industrial scale.

1. Introduction

In recent years, environmental pollution has induced great concerns and discussion in international and domestic societies. Volatile organic compounds (VOCs) are a class of chemical substances widely present in various fields, such as chemical industries, automotive exhaust emissions, and solvent utilization. The emissions of these compounds to the atmosphere not only cause environmental pollution, but also pose a serious threat to human health [1,2]. Therefore, the emission of VOCs

has attracted widespread attention in environmental protection and public health. However, chlorinated volatile organic compounds (CVOCs), such as dichloromethane (DCM), dichloroethane (DCE), and trichloroethylene (TCE), have strong toxicity and high chemical stability, and are difficult to biodegrade and easily accumulate in organisms. Such CVOCs exhibit strong carcinogenic, teratogenic, and mutagenic effects [3,4]. Therefore, it is highly desired to control the emissions of VOCs and CVOCs. Catalytic oxidation is one of the most effective methods for the removal of VOCs and CVOCs, which focuses on

* Corresponding author at: Beijing Key Laboratory for Green Catalysis and Separation, Key Laboratory of Beijing on Regional Air Pollution Control, Key Laboratory of Advanced Functional Materials, Education Ministry of China, China.

E-mail addresses: jgdeng@bjut.edu.cn (J. Deng), hxdai@bjut.edu.cn (H. Dai).

exploring the improvements in catalytic performance and stability of the catalysts so as to make them suitable for applications under complex industrial conditions [5–7].

Acidic sites are usually introduced into the catalysts to increase surface acidity, which can be beneficial for the adsorption of CVOCs molecules and the activation of C–Cl bonds, hence enhancing their catalytic activities at low temperatures. Catalytic oxidation of CVOCs typically involves two consecutive steps: (i) the C–Cl bonds are cleaved at the Brønsted acid sites (BAS) and/or the surface oxygen vacancies; and (ii) VOCs or intermediates undergo deep oxidation at the Lewis acid sites (LAS) [8,9]. Up to now, a large number of studies have shown that modification of a molecular sieve after the surface acid treatment can significantly increase the concentrations of BAS and LAS on the catalyst surface, thereby improving the selectivities toward HCl, Cl₂, and CO₂. For example, Yu et al. [10] modified the surface of the Ru/TiO₂ catalysts with H₃PW₁₂O₄₀ (HPW), and found that the HPW-modified Ru/TiO₂ catalyst (Ru/HPW-TiO₂) contained more 1,2-dichloroethane adsorption sites that could promote the oxidation of 1,2-dichloroethane, and this catalyst exhibited excellent water resistance. Compared with Ru/TiO₂, the Ru/HPW-TiO₂ catalyst possessed more BAS and showed better selectivities toward HCl and Cl₂, but BAS tended to adsorb toluene in mixed VOC oxidation. The introduction of BAS inevitably weakens the strength of LAS and hinders the deep oxidation of CVOCs, hence catalytic activity of Ru/HPW-TiO₂ was not as good as that of Ru/TiO₂. Transition metal oxides possess a good ability to break the C–Cl bonds and high catalytic activities in the oxidation of CVOCs. At the same time, zeolites with abundant acid sites can enhance their resistance to chlorine poisoning. Therefore, the hybrid catalyst system of transition metal oxides and zeolites has received widespread attention [11]. For instance, the Cr–CeO₂/HZSM-5 [12], Mn/ZSM-5 [13], Mn_xCe_{1-x}O₂/H-ZSM-5 [14], and Fe/ZSM-5 [15] catalysts performed well in the oxidation of CVOCs. Li et al. [16] designed new tandem PtSn/CeO₂&Mn/ZSM-5 catalysts, and studied their catalytic performance for the oxidation of multi-component CVOCs (TCE + toluene), in which the former PtSn/CeO₂ catalyst was mainly responsible for the deep oxidation of toluene at low temperatures, while the latter Mn/ZSM-5 catalyst was responsible for the oxidation of TCE. Although this strategy achieved a significant efficiency in toluene and TCE oxidation, it still produced toxic by-products, such as chlorobenzene (CB) and 4-chlorotoluene.

Excessive acid sites can lead to a decrease in redox ability of a catalyst, thereby interfering the deep oxidation of CVOCs. When the redox ability is too strong, however, it is easy to form polychlorinated by-products, thus decreasing the desired product selectivity. Therefore, it is of great significance to construct the catalysts with excellent redox ability and rich acidic sites for the synergistic removal of VOCs and CVOCs. Zeolites are widely used as catalysts for CVOCs oxidation due to their high thermal stability and flexible ion exchange ability. The pore structure of HZSM-5 perfectly matches the geometry of aromatic hydrocarbons, and HZSM-5 is considered as a suitable catalyst for the conversion of chlorinated aromatic hydrocarbons [17]. Nevertheless, HZSM-5 possesses a strong acidity, while excessive acidic sites can also induce coke deposition and chlorine poisoning on the surface of the zeolite, thereby deactivating the catalyst. Therefore, it is important to regulate appropriate acidic sites of a catalyst so as to improve its deep oxidation performance. Sn-BEA or Sn-MFI possesses a certain amount of LAS [18], and in addition, the reduction of Sn⁴⁺ to Sn²⁺ can form oxygen vacancies at lower temperatures, which attracts much attention in heterogeneous catalysis [19].

In this work, we prepared the Sn-doped Silicalite-1-supported Ru (Ru@Silicalite-1-Sn-x, and x is the molar ratio of Sn/Si) catalysts with close coupled multi active sites by adjusting their microstructures, and evaluated their catalytic oxidation performance in the oxidation of multicomponent VOCs (toluene and DCM). The surface compositions, acidity, and redox behaviors of the as-prepared catalysts were characterized using various techniques. Catalytic activities, stability, and selectivities of the samples were further investigated, and the involved

reaction mechanisms of toluene and DCM oxidation over the catalysts were also explored. It was found the high concentrations of surface oxygen vacancies, controllable BAS and LAS, atom-dispersed Ru and close coupled multiple active sites were the main reasons for the excellent catalytic performance of Ru@Silicalite-1-Sn-50. Our research findings are expected to provide a useful guidance for the design of the catalysts with excellent activity, selectivity, durability, and functionality for mixed VOCs and CVOCs oxidation.

2. Experimental

2.1. Catalyst preparation

2.1.1. Preparation of Ru(NH₂CH₂CH₂NH₂)₃Cl₃ solution

43.12 mg of RuCl₃, 9 mL of deionized water, and 1 mL of ethylenediamine were mixed and stirred at 50 °C overnight, obtaining the Ru (NH₂CH₂CH₂NH₂)₃Cl₃ solution.

2.1.2. Preparation of Silicalite-1 and Silicalite-1-Sn

In a typical preparation process, 10.41 g of tetraethylorthosilicate (TEOS) was added into a mixture of 16.25 g of tetrapropylammonium hydroxide (TPAOH, 25 wt%) solution and 19.28 mL of deionized water. After continuous stirring for 10 h, TEOS was fully hydrolyzed. The above mixture was then transferred into a 100-mL Teflon-lined autoclave for thermal treatment at 170 °C for 72 h. After the solids were centrifuged, dried, and calcined at 550 °C for 6 h, Silicalite-1 was obtained. The synthesis process of Silicalite-1-Sn was similar to that of Silicalite-1. The Sn (SnCl₄·5 H₂O) source was introduced into the above solution to prepare the Silicalite-1-Sn samples with the n(Si)/n(Sn) molar ratios of 20–100, which were denoted as Silicalite-1-Sn-x (x was the molar ratio of Si/Sn in the initial synthesis gel).

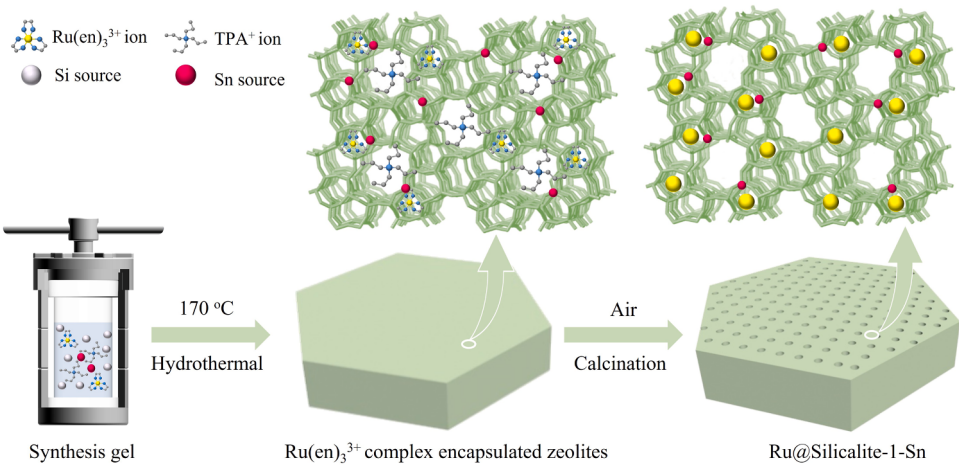
2.1.3. Preparation of Ru@Silicalite-1, Ru@Silicalite-1-Sn-x, and Ru/SnO₂/Silicalite-1

As illustrated in Scheme 1, the preparation processes of Ru@Silicalite-1 and Ru@Silicalite-1-Sn were similar to that of Silicalite-1, but only one precursor (Ru(NH₂CH₂CH₂NH₂)₃Cl₃) and two precursors (Ru(NH₂CH₂CH₂NH₂)₃Cl₃ and SnCl₄·5 H₂O) were separately added to the above TPAOH- and TEOS-containing aqueous solution, which were also transferred to a 100-mL Teflon-lined autoclave for thermal treatment at 170 °C for 72 h. After the subsequent centrifugation filtering, drying, and calcination at 550 °C for 4 h, the Ru@Silicalite-1 and Ru@Silicalite-1-Sn-x samples were obtained.

The Ru/SnO₂/Silicalite-1 sample was fabricated using the wetness impregnation method. 0.5 g of the calcined Silicalite-1 and 58.3 mg of SnCl₄·5 H₂O were impregnated with 3.46 mL of RuCl₃ aqueous solution (0.01 mol/L). The obtained solid was first dried overnight and then calcined at 550 °C for 4 h to obtain the Ru/SnO₂/Silicalite-1 sample. The actual metal Ru loadings in the supported Ru samples were determined using the inductively coupled plasma-atomic emission spectroscopic (ICP-AES) technique, and their results are shown in Table S2.

2.2. Catalyst characterization

ICP-AES, X-ray diffraction (XRD), Raman spectroscopy, nuclear magnetic resonance (NMR), ultraviolet-visible spectroscopy (UV-vis), N₂ adsorption-desorption measurements (BET), high-angle annular dark field-scanning transmission electron microscopy (HAADF-STEM), X-ray photoelectron spectroscopy (XPS), electron paramagnetic resonance (EPR), gas chromatography-mass spectroscopy (GC-MS), oxygen, ammonia or volatile organic compound temperature-programmed desorption (O₂, NH₃- or VOC-TPD), temperature-programmed surface reaction (TPSR), H₂ temperature-programmed reduction (H₂-TPR), Fourier transform infrared spectroscopy (Py-FTIR), and in situ diffuse reflectance Fourier transform infrared spectroscopy (in situ DRIFTS) were used to characterize physicochemical properties of



Scheme 1. The illustrative synthesis procedure of the Ru@Silicalite-1-Sn sample.

the as-prepared samples. The detailed characterization procedures can be seen in the [Supplementary material](#).

2.3. Catalytic performance measurement

Catalytic activities for the oxidation of toluene and/or DCM of the as-prepared samples were evaluated in a fixed-bed quartz tubular micro-

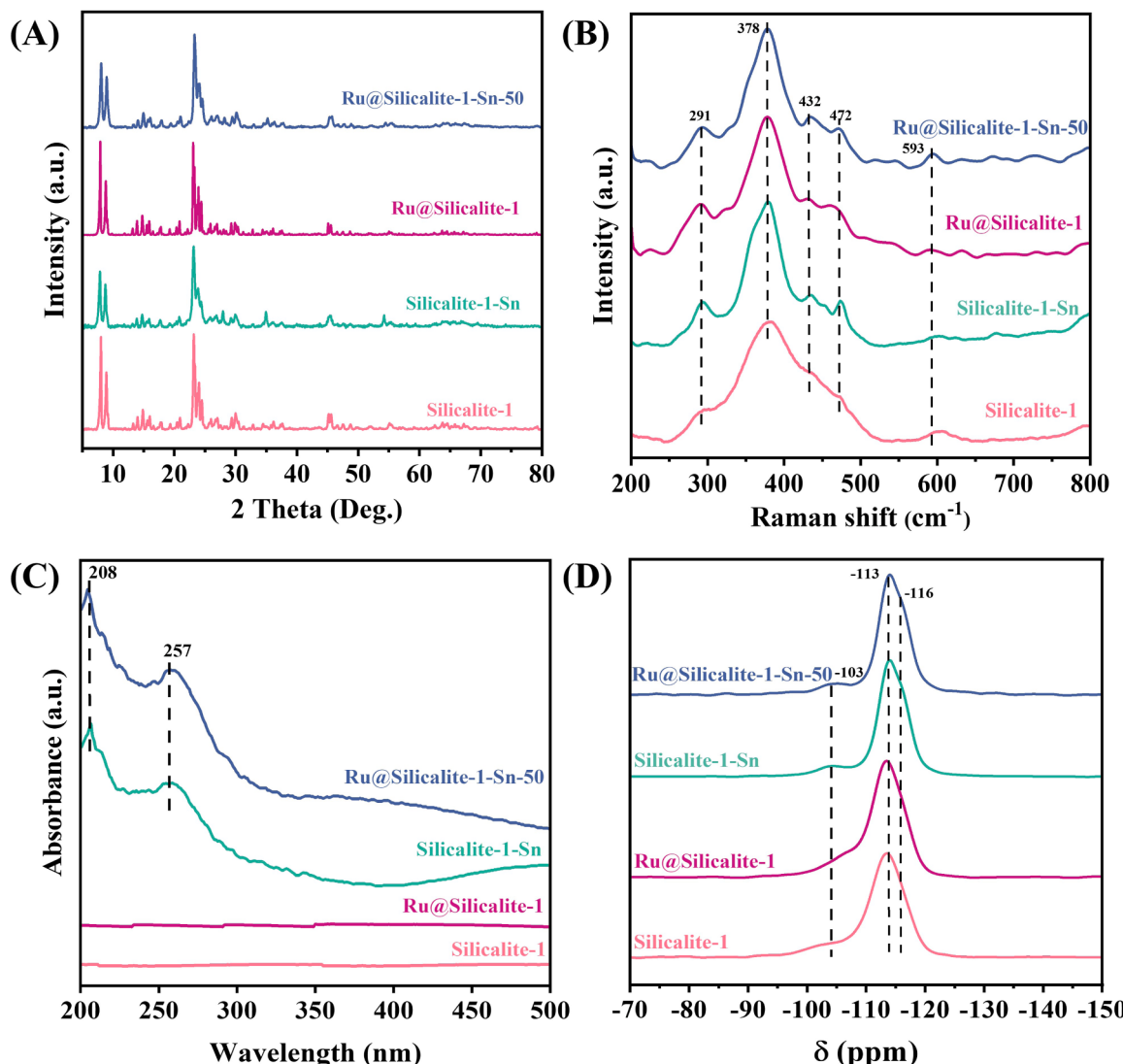


Fig. 1. (A) XRD patterns, (B) Raman spectra, (C) NMR spectra, and (D) UV–vis diffuse reflectance spectra of the as-prepared samples.

reactor. The reaction feedstock gas mixture was composed of (1000 ppm toluene + 20 vol% O₂ + N₂ (balance)) with or without 500 ppm DCM and/or (500 ppm DCM + 20 vol% O₂ + N₂ (balance)), and the space velocity (SV) was 40,000 mL/(g h). A gas chromatography (Agilent, GC7890) was used to analyze the concentrations of the reactants and products. The detailed catalytic activity evaluation procedures were described in the [Supplementary material](#).

3. Results and discussion

3.1. Physical properties

[Fig. 1A](#) shows XRD patterns of the as-prepared samples. There were diffraction peaks assignable to an MFI zeolite structure (JCPDS PDF# 44-0003), and no XRD signals attributable to the SnO₂ crystal or Ru phase were recorded. This result indicates that the addition of Sn and/or Ru does not exert a significant effect on the crystallization of Silicalite-1. As shown in [Table S1](#), the unit cell volume of Silicalite-1 increased with the doping of Sn. This means that the tetrahedral Si atoms (atomic radius = 1.17 Å) of the lattice are isomorphically replaced by the bigger Sn atoms (atomic radius = 1.58 Å), resulting in the expansion of the crystal lattice. Therefore, the above results indirectly indicate that part of Sn atoms are incorporated into the matrix of the zeolite.

The laser Raman technique was employed to gain bond information of the as-prepared samples, and their corresponding spectra are shown in [Fig. 1B](#). The bands at 291 and 472 cm⁻¹ were due to the bending vibrations of the six- ring and four-membered rings in the zeolite, respectively. The bands at 378 and 432 cm⁻¹ were attributable to the stretching vibration of the Si—O—Si bonds and the asymmetric stretching vibration of the Sn—O—Si bonds in each sample [20], respectively. UV-vis spectroscopy can be used to investigate coordination states of the metals in heteroatomic molecular sieves. As shown in [Fig. 1C](#), the recording of an absorption band at 208 nm of the Silicalite-1-Sn and Ru@Silicalite-1-Sn-50 samples indicated the formation of a tetrahedral coordination, and in addition, an additional band at 257 nm signified the presence of a small amount of hexa-coordinated tin in the samples [21,22]. The above observations were consistent with the Raman results. The Sn 3d XPS signal was shifted toward a higher binding energy, which confirmed the formation of a tetrahedral coordination of Sn—O—Si bonds ([Fig. S1\(B\)](#)) [23]. In addition, as shown in the partially enlarged XRD patterns of the samples ([Fig. S2](#)), diffraction peaks of the samples were shifted to lower angles after the addition of Sn, indicating that the lattice cell became larger, which also confirms the formation of Sn—O—Si bonds. No signals were observed at wavelengths above 300 nm, indicating the absence of the polymerized tin species in the Silicalite-1-Sn and Ru@Silicalite-1-Sn-50 samples [24].

In order to determine the chemical environments of Si and Sn atoms, ²⁹Si MAS NMR analysis on the as-prepared samples was performed, and their results are shown in [Fig. 1D](#). All of the zeolitic samples exhibited similar signals at -103 and -113 ppm, which were assigned to the differently coordinated Si species of (SiO)₃SiOH (Q³) and (SiO)₄Si (Q⁴) [25], respectively. Importantly, Silicalite-1-Sn and Ru@Silicalite-1-Sn-50 displayed shoulder peaks around -116 ppm, which was due to the induction effect of Sn atoms on the adjacent Si atoms [26]. Therefore, this result was another piece of important evidence for the presence of the tetrahedral Sn species (isomorphically replacing the skeleton Si atoms).

The N₂ adsorption–desorption isotherms and pore-size distributions of the samples are presented in [Fig. S3](#). These as-prepared samples displayed type-I isotherms and sharp adsorption N₂ uptakes in the low relative pressure range ($p/p_0 < 0.1$), which confirmed the formation of typical micropores. [Table S2](#) shows specific surface areas, pore volumes, and pore sizes of the samples. These samples possessed large surface areas (> 400 m²/g) and could provide rich adsorption sites for VOCs and oxygen molecules. Compared with Silicalite-1 and Silicalite-1-Sn, surface areas and pore volumes were lower after the loading of Ru NPs, a

result possibly due to the partial blocking of the micropores by the Ru species. The porous structure with a higher surface area was beneficial for the enhancement in adsorption and mass transfer of reactants molecules, and the nanosized skeleton surface was favorable for high dispersion of Ru single atom that could strengthen the interaction between Ru single atom and support. Furthermore, the porous channel structure was also conducive to reducing formation of the by-products.

[Fig. S4\(A–D\)](#) presents SEM images of the Ru@Silicalite-1 and Ru@Silicalite-1-Sn-50 samples. The Ru@Silicalite-1 sample showed a hexagonal prism morphology with a particle size of approximately 250 nm. After the doping of Sn, morphology of the sample was changed to an ellipsoidal shape from NPs accumulation, with the average size being 500 nm. In order to obtain the information of metal species distribution, TEM images of the Ru@Silicalite-1 sample are shown in [Fig. S5\(A–D\)](#). It is worth noting that, Ru NPs were well distributed in Ru@Silicalite-1, and the measured lattice spacing of the noble metal NPs was 0.319 nm, corresponding to the (110) lattice plane of RuO₂, and the average size of Ru NPs was 4.12 nm. Compared with Ru@Silicalite-1, however, no Ru NPs were observed in Ru@Silicalite-1-Sn-50, which confirmed that the doping of Sn increased the dispersion of Ru. Besides, no SnO₂ NPs were found, indicating that the Sn species were uniformly distributed in the framework of the molecular sieve Silicalite-1. In addition, as shown in [Fig. S6\(B and D\)](#), the lattice spacing of the Ru@Silicalite-1-Sn-50 sample with the Si–Sn bonds was significantly smaller than that of the Ru@Silicalite-1 sample with Si–Si bonds. At the same time, the formation of Si–Sn bonds and Ru single atoms simultaneously constituted the tightly coupled multiple active sites in the Ru@Silicalite-1-Sn-50 sample. This result was in good consistency with the Raman and NMR characterization results.

As can be seen from Ac-HAADF–STEM images of the Ru@Silicalite-1-Sn-50 sample ([Fig. 2A–C](#)), the recording of bright spots in the above images indicates that the Ru species are dispersed in single atoms. Shown in [Fig. 2D](#) are the EDS elemental mappings of the Ru@Silicalite-1-Sn-50 sample. Apparently, the Ru and Sn elements were evenly distributed in the Ru@Silicalite-1-Sn-50 sample. Further verification of the dispersion state of Ru in the Ru@Silicalite-1-Sn-50 sample was carried out using the operando diffuse reflectance infrared spectroscopy with CO probe molecules (CO-DRIFTS). As shown in [Fig. S7](#), there were three characteristic absorption bands, in which the bands at 2173 and 2119 cm⁻¹ were attributed to the adsorption of gas-phase CO, and the one at 2058 cm⁻¹ was ascribed to the linear bonding of the atomically dispersed Ru species and CO, forming a dicarbonyl Ru^{δ+}(CO)₂ species [27,28].

3.2. Catalytic performance

Catalytic performance of the samples were measured for the oxidation of 1000 ppm toluene, 500 ppm DCM or (1000 ppm toluene + 500 ppm DCM) at a space velocity (SV) of 40,000 mL/(g h). [Fig. S8\(A, B\)](#) show the conversions of single toluene and single DCM at different temperatures. Obviously, Silicalite-1 and Silicalite-1-Sn showed poor catalytic activities for the oxidation of toluene or DCM. After Ru was loaded on the surface of Silicalite-1 or Silicalite-1-Sn, catalytic activity of the sample was significantly enhanced, and the metal-encapsulated samples exhibited better catalytic performance than the metal-supported counterparts, which might be attributable to the fact that tightly coupled redox and acidic centers were generated in the Ru@Silicalite-1-Sn-50 sample. The Sn species in the Ru@Silicalite-1-Sn-50 sample were uniformly distributed in the skeleton of the Silicalite-1 zeolite, while most of the Sn species in the Ru/SnO₂/Silicalite-1 sample were dispersed on the surface of the sample, which blocked some of the pores and affected the mass transfer. The Ru@Silicalite-1-Sn-50 sample possessed a more amount of the acid sites compared to the Ru/SnO₂/Silicalite-1 sample, which was favorable for the adsorption and activation of DCM and toluene. In addition, the Ru single atom in Ru@Silicalite-1-Sn-50 was favorable for the adsorption and activation of

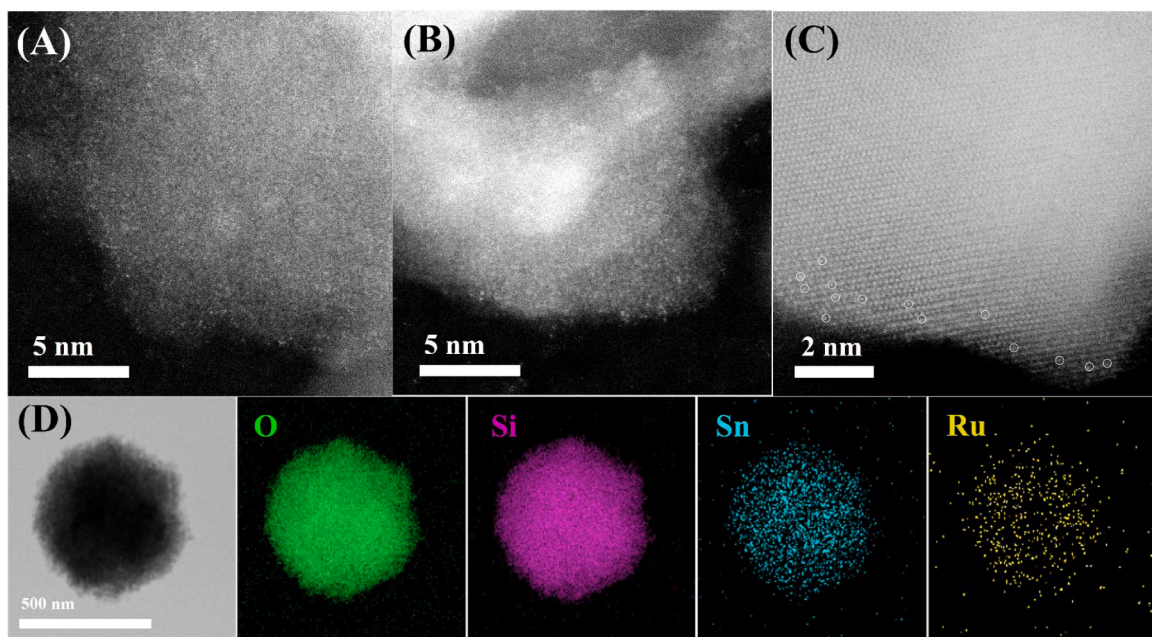


Fig. 2. (A–C) Ac-HAADF–STEM images of Ru@Silicalite-1-Sn-50 and (D) EDS elemental mappings of Ru@Silicalite-1-Sn-50.

O_2 , which resulted in excellent activity of this catalyst. In order to compare catalytic activities of all of the samples, we used the temperatures ($T_{50\%}$ and $T_{90\%}$) at 50 and 90% toluene or DCM conversions (Tables 1 and 2). catalytic DCM oxidation activities of Ru@Silicalite-1 ($T_{90\%} = 394^\circ C$) and Ru@Silicalite-1-Sn-50 ($T_{90\%} = 325^\circ C$) and catalytic toluene oxidation activities of Ru@Silicalite-1 ($T_{90\%} = 291^\circ C$), Ru@Silicalite-1-Sn-50 ($T_{90\%} = 245^\circ C$) were totally different. The loading of Sn species on Silicalite-1 could increase the number of the Brønsted and Lewis acid sites, and modify the chemical environment of the formed interface, thus prohibiting adsorption of the Cl species. The Ru single atom interacted with the support to generate the active RuSn–support interface, which was beneficial for deep oxidation of CVOCs. In addition, the Ru single atom was in favor of adsorbing and activating O_2 , and the strong interaction between the highly dispersed single-atom Ru and Sn species gave rise to the enhancement in anti-Cl poisoning of the Ru species in the reaction of the Cl-containing reactant. To further demonstrate the effect of Sn content on catalytic activity, we measured catalytic activities of the samples with different $n(Si)/n(Sn)$ molar ratios (Fig. S9). With the drop in $n(Si)/n(Sn)$ molar ratio, catalytic activity of the sample was slightly improved. When $n(Si)/n(Sn) = 20$, however, catalytic activity was decreased. The enhancement in catalytic DCM or toluene oxidation activity of the Sn-doped sample was due to the electronic interaction of Ru and Sn and the synergistic effect of tightly coupled multiple active sites. Since various VOCs are present in the actual industrial environments, catalytic performance of the

samples over the mixed VOCs (e.g., (1000 ppm toluene + 500 ppm DCM)) was investigated. Fig. 3 A and B shows the conversions of DCM and toluene in the mixed VOCs at different temperatures, in which the changing trend of mixed VOCs conversions was similar to that of individual VOC conversions. Furthermore, the conversion temperature of mixed VOCs slightly increased compared with the single component VOCs, indicating the presence of competitive adsorption of toluene and DCM on the sample surface. Ru@Silicalite-1-Sn-50 exhibited the best catalytic activity ($T_{90\%(\text{toluene})} = 287^\circ C$ and $T_{90\%(\text{DCM})} = 361^\circ C$) among all of the samples. To evaluate the catalytic activity more accurately, turnover frequencies (TOFs) of the samples were calculated for the oxidation of toluene at $170^\circ C$ or DCM at $200^\circ C$: $\text{TOF}_{\text{Ru}} = X V / N_{\text{Ru}} D_{\text{Ru}}$, where X (%) represents the toluene or DCM conversion, V (mol/s) is the toluene or DCM flow rate, N_{Ru} (mol) is the Ru molar content in the sample, and D_{Ru} (%) is the dispersion of Ru on the surface of the sample. The TOFs of toluene or DCM oxidation in mixed VOCs over the Ru-loaded samples are shown in Tables 1 and 2, respectively. The TOF_{Ru} ($0.98 \times 10^{-3} \text{ s}^{-1}$) of the Ru@Silicalite-1-Sn-50 sample for toluene oxidation in mixed VOCs at $170^\circ C$ was the highest, much higher than that ($0.43 \times 10^{-3} \text{ s}^{-1}$) of the Ru/SnO₂/Silicalite-1 sample and that ($0.26 \times 10^{-3} \text{ s}^{-1}$) of the Ru@Silicalite-1 sample. The TOF_{Ru} for DCM oxidation in mixed VOCs decreased in the order of Ru@Silicalite-1-Sn-50 ($0.46 \times 10^{-3} \text{ s}^{-1}$) > Ru/SnO₂/Silicalite-1 ($0.24 \times 10^{-3} \text{ s}^{-1}$) > Ru@Silicalite-1 ($0.2 \times 10^{-3} \text{ s}^{-1}$).

In addition, the specific reaction rates of DCM oxidation in mixed

Table 1

Catalytic activities for the oxidation of toluene in the single VOC or mixed VOCs (toluene + DCM), TOF_{Ru} , and apparent activation energies (E_a) of the samples at SV = 40,000 mL/(g h).

Sample	Catalytic activity				Oxidation of toluene in mixed VOCs at $170^\circ C$		E_a for the oxidation of toluene in mixed VOCs (kJ/mol)	
	Toluene oxidation (Single VOC)		Toluene oxidation (Mixed VOCs)		Specific reaction rate ($\mu\text{mol}/(\text{g}_{\text{cat}} \text{s})$)	TOF_{Ru} ($\times 10^{-3} \text{ s}^{-1}$)		
	$T_{50\%}$ ($^\circ C$)	$T_{90\%}$ ($^\circ C$)	$T_{50\%}$ ($^\circ C$)	$T_{90\%}$ ($^\circ C$)				
Silicalite-1	-	-	-	-	-	-	117	
Silicalite-1-Sn	-	-	-	-	-	-	109	
Ru@Silicalite-1	245	291	267	325	2.65	0.26	62	
Ru@Silicalite-1-Sn-50	202	245	236	287	9.67	0.98	44	
Ru/SnO ₂ /Silicalite-1	238	274	257	314	4.29	0.43	54	

Table 2

Catalytic activities for the oxidation of DCM in the single VOC or mixed VOCs (toluene + DCM), TOF_{Ru} , and apparent activation energies (E_a) of the samples at $\text{SV} = 40,000 \text{ mL}/(\text{g h})$.

Sample	Catalytic activity				Oxidation of DCM in mixed VOCs at 200 °C		E_a for the oxidation of DCM in mixed VOCs (kJ/mol)	
	DCM oxidation (Single VOC)		DCM oxidation (Mixed VOCs)		Specific reaction rate ($\mu\text{mol}/(\text{g}_{\text{cat}} \text{s})$)	$\text{TOF}_{\text{Ru}} (\times 10^{-3} \text{s}^{-1})$		
	$T_{50\%}$ (°C)	$T_{90\%}$ (°C)	$T_{50\%}$ (°C)	$T_{90\%}$ (°C)				
Silicalite-1	-	-	-	-	-	-	124	
Silicalite-1-Sn	-	-	-	-	-	-	122	
Ru@Silicalite-1	318	394	368	433	2.02	0.2	65	
Ru@Silicalite-1-Sn-50	270	325	301	361	3.84	0.46	48	
Ru/SnO ₂ /Silicalite-1	303	371	355	408	2.40	0.24	63	

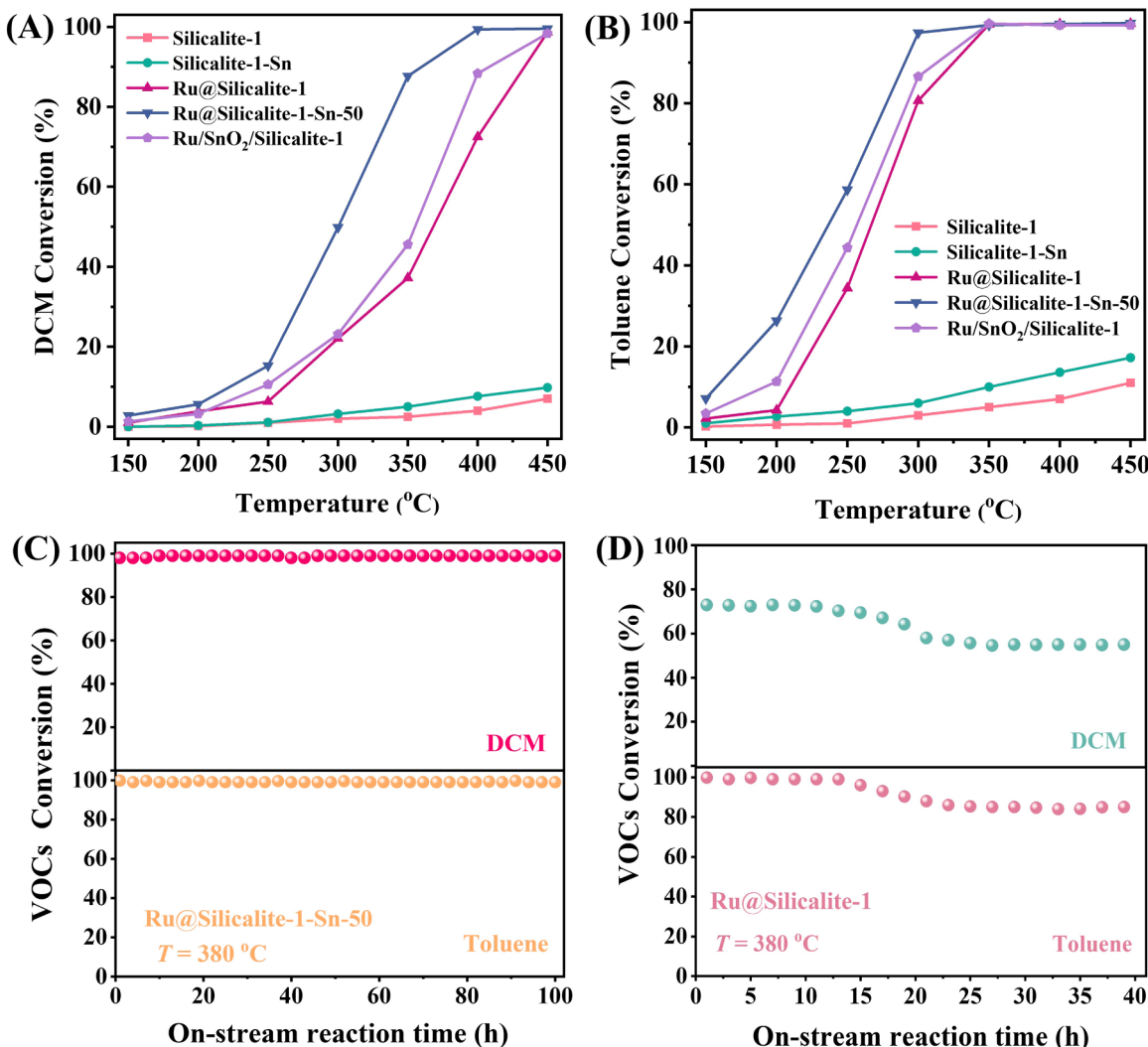


Fig. 3. (A) DCM and (B) toluene conversions versus temperature over the samples in the oxidation of mixed VOCs at $\text{SV} = 40,000 \text{ mL}/(\text{g h})$, DCM and toluene conversions as a function of on-stream reaction time over (C) Ru@Silicalite-1-Sn-50 and (D) Ru@Silicalite-1 at 380 °C and $\text{SV} = 40,000 \text{ mL}/(\text{g h})$.

VOCs over the samples at 200 °C were calculated. Obviously, the changing trend in specific reaction rate was the same as that in catalytic activity of the samples. By comparing catalytic activities of the typical sample (Ru@Silicalite-1-Sn-50) presented in this work and the catalysts reported in the literature (Table S3), one can see that catalytic DCM oxidation activity of our Ru@Silicalite-1-Sn-50 sample is superior to those of most of the catalysts reported in the literature, although the multicomponent VOCs (toluene and DCM) were used as reactants in our

study. The specific reaction rate ($3.84 \mu\text{mol}/(\text{g}_{\text{cat}} \text{s})$) of Ru@Silicalite-1-Sn-50 was higher than those ($\leq 3.12 \mu\text{mol}/(\text{g}_{\text{cat}} \text{s})$) of Pt/Al₂O₃ [29], Ir-OMS-2 [30], Cr-Co@ZSM-5 [31], Ru/Ti_{0.6}Sn_{0.4} [19], 0.01Pt-20Co/HZSM-5 [32], Ru@ZSM-5 [33], and RuO₂-WO₃/Sn_{0.2}Ti_{0.8}O₂ [34], and but lower than that ($6.25 \mu\text{mol}/(\text{g}_{\text{cat}} \text{s})$) of PO_x-CeO₂-0.2 [35] and that ($6.32 \mu\text{mol}/(\text{g}_{\text{cat}} \text{s})$) of 2.0Pt/15Al-CeO [36].

Apparent activation energies (E_a) of mixed VOCs oxidation over the

as-obtained samples were calculated. As shown in Fig. S10(A, B), the sequence of E_a for the oxidation of toluene in mixed VOCs followed the order of Silicalite-1 (117 kJ/mol) > Silicalite-1-Sn (109 kJ/mol) > Ru@Silicalite-1 (62 kJ/mol) > Ru/SnO₂/Silicalite-1 (54 kJ/mol) > Ru@Silicalite-1-Sn-50 (44 kJ/mol), and that for the oxidation of DCM in mixed VOCs followed the order of Silicalite-1 (124 kJ/mol) > Silicalite-1-Sn (122 kJ/mol) > Ru@Silicalite-1 (65 kJ/mol) > Ru/SnO₂/Silicalite-1 (63 kJ/mol) > Ru@Silicalite-1-Sn-50 (48 kJ/mol), which was in line with their changing trend in catalytic activity for the oxidation of mixed VOCs.

During the oxidation processes of mixed VOCs, some toxic products can be generated. Hence, it is necessary to analyze the products formed over the different samples. Only the dechlorinated by-product (CH₃Cl) and polychlorinated by-products (CHCl₃, CCl₄, and C₆H₅Cl) were detected in the oxidation of mixed VOCs, but no other by-products were observed due to the very low concentrations (beyond the chromatographic detection limit). The concentrations of by-products formed over Ru@Silicalite-1 and Ru/SnO₂/Silicalite-1 showed a first-increasing and then-decreasing trend with the rise in temperature. When the reaction temperature increased to 300–350 °C, the concentrations of by-products gradually decreased (Fig. 4A–D). In addition, the lowest concentration of by-products were found over the Ru@Silicalite-1-Sn-50 sample. The concentration of Cl₂ gradually increased over Ru@Silicalite-1 and Ru/SnO₂/Silicalite-1, which indicates decomposition of the organic by-products at high temperatures and occurrence of the Deacon reaction (Cl₂ concentration gradually decreased with the rise in temperature). Lower Cl₂ concentration was detected over the Ru@Silicalite-1-Sn-50 sample. According to the literature [37], Cl species could react with aromatic frameworks to generate chlorobenzene (CB) through the electrophilic substitution. As shown in Fig. 4C, the concentration of CB formed over Ru@Silicalite-1-Sn-50 was the lowest (< 3 ppm) during the reaction process. We speculate that the final

product of the Cl species was HCl, which may be related to its rich acid sites measured using the Py-FTIR technique. It has been reported that the LAS was more active in the deep oxidation of CVOCs than the BAS [38]. CO₂ is one of the target products in the oxidation of VOCs. The CO₂ yield over the Ru@Silicalite-1-Sn-50 sample was higher than that over the other two samples (Fig. 4F), which was in good agreement with the changing trend in toluene or DCM conversion. This result indicates that there are very few toluene and DCM oxidized into organic by-products over the Ru@Silicalite-1-Sn-50 sample.

The durability of a catalyst is one of the most important indexes for industrial applications. It has been demonstrated that zeolitic catalysts are prone to coke deposition, and toxic substances related to the Cl species are easily formed during the oxidation processes of chlorinated aromatic hydrocarbons, hence leading to the catalyst deactivation [39]. As shown in Fig. 3C, we conducted thermal stability experiments using the Ru@Silicalite-1-Sn-50 sample. Catalytic activity of the sample for mixed VOCs oxidation did not decrease within 100 h (380 °C) of on-stream reaction and remained stable at a conversion of ca. 99%. We also tested the stability of the Ru@Silicalite-1-Sn-50 sample at 280 °C and SV = 40,000 mL/(g h), and the results are shown in Fig. S11. Obviously, the catalytic activity of this sample for the oxidation of mixed VOCs did not decrease within 40 h of reaction. However, catalytic activity of the Ru@Silicalite-1 sample decreased by ca. 15% in the 40 h stability test (Fig. 3D). This result might be related to the fact that the Ru@Silicalite-1-Sn-50 sample possesses good tightly coupled redox sites and abundant acidic sites, which is in good agreement with the results of O₂- and HCl-TPD characterization (see below). That is to say, coking and poisoning of the Ru@Silicalite-1-Sn-50 catalyst were greatly inhibited. In addition, we also explored the effect of water vapor on catalytic activity of the Ru@Silicalite-1-Sn-50 sample. As shown in Fig. S12(A), the introduction of either 3 or 5 vol% water vapor to the reaction system increased the conversion of DCM by ca. 14%, but the DCM conversion

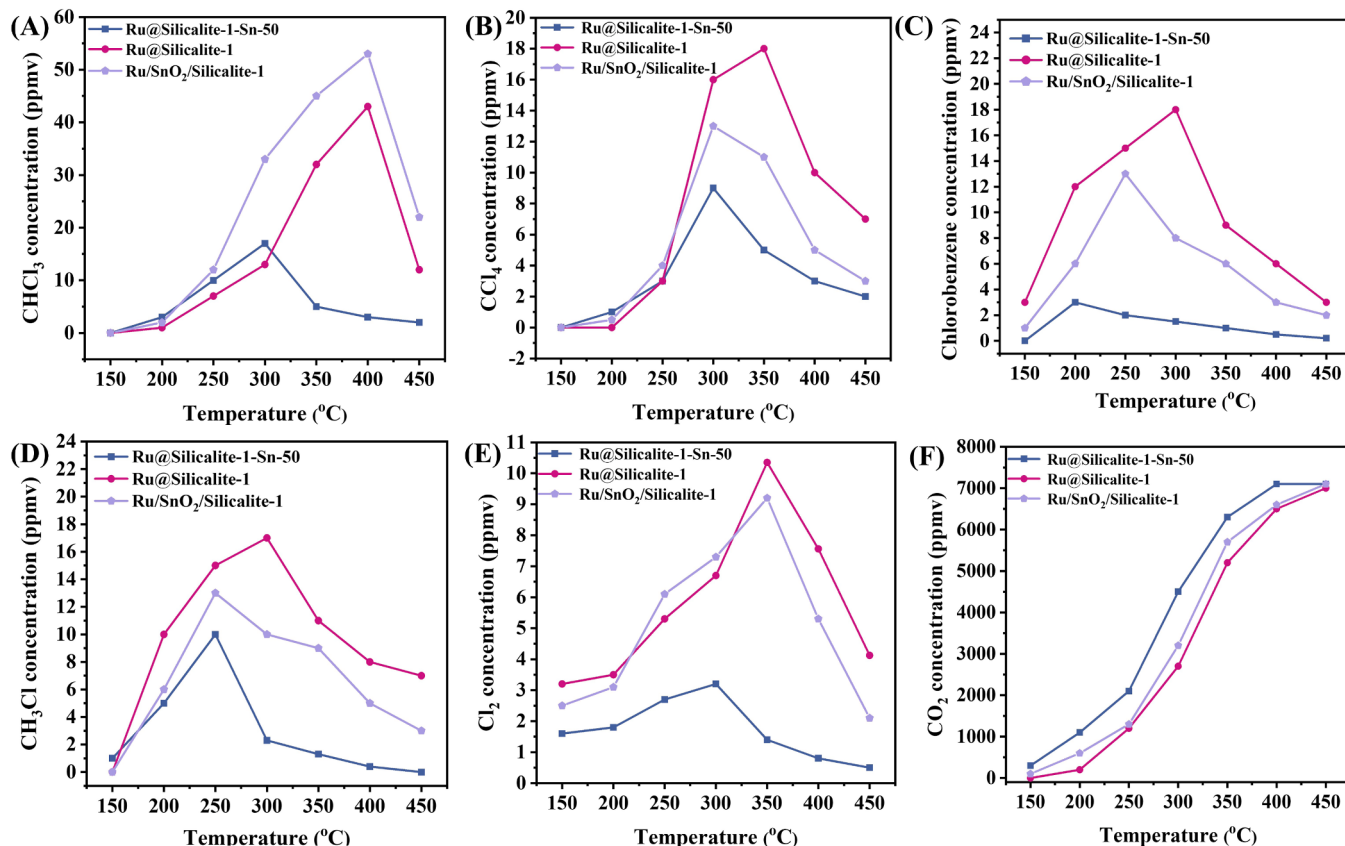


Fig. 4. Product concentration as a function of temperature over the as-obtained samples.

returned to its initial level after cutting off the water vapor provision. Moreover, the introduction of water vapor did not exert a significant effect on catalytic activity for toluene oxidation, which could maintain a high conversion level (Fig. S12(B)). The above results demonstrate that the Ru@Silicalite-1-Sn-50 sample possessed good water resistance in the oxidation of DCM and toluene. In order to understand the effect of water on catalytic activity, we measured catalytic activities of the resulting samples for the oxidation of DCM and toluene when 3.0 vol% of water vapor was introduced into the feedstock, and their results are shown in Fig. S12(C, D). Apparently, the addition of water promoted the oxidation of DCM over all of the samples (for example, the $T_{50\%}$ decreased by 20 °C and the $T_{90\%}$ decreased by 10 °C over Ru@Silicalite-1-Sn-50), but the oxidation of toluene was not significantly influenced by water introduction.

3.3. Redox property, acidity, metal oxidation state, surface element composition, and oxygen species

In catalytic reactions, redox behaviors and molecular oxygen adsorption and activation of/on catalysts are important. The oxygen desorption behaviors of the samples were measured using the O₂-TPD technique, and their O₂-TPD profiles are shown in Fig. 5A. The desorption peaks at 50–300 °C were assigned to the surface physical and/or chemical adsorbed oxygen (O_{ads}), the ones at 300–600 °C were attributed to the surface lattice oxygen, and the ones above 600 °C were ascribed to the bulk lattice oxygen (O_{latt}). Compared with Silicalite-1 and Silicalite-1-Sn, the addition of Ru increased the amount of O_{ads}, thus improving catalytic activity of the sample. According to the Wigner's spin selection rule, activation of the ground-state O₂ into the reactive oxygen species is beneficial for the oxidation reaction [40]. The

results (Fig. 5B) of EPR characterization confirmed the presence of oxygen vacancies (O_{vac}) in/on the Ru@Silicalite-1 and Ru@Silicalite-1-Sn-50 samples. The signal near $g = 2.003$ was due to the O_{vac} of unpaired electrons caused by the defect of the sample. The Ru@Silicalite-1-Sn-50 sample possessed a higher oxygen vacancy concentration than that of the Ru@Silicalite-1 sample, which helped to adsorb oxygen molecules and produced a more amount of the reactive oxygen species. As for the surface oxygen species, the recorded O 1 s XPS spectra (Fig. 5C) could be divided into two components, assignable to the O_{ads} species at binding energy (BE) = 531.7 eV and the O_{latt} species at BE = 530.8 eV. As listed in Table S4, the descending order in surface O_{ads}/O_{latt} molar ratio was Ru@Silicalite-1-Sn-50 (1.49) > Ru@Silicalite-1 (0.86) > Silicalite-1-Sn (0.42) > Silicalite-1 (0.35), in which the Ru@Silicalite-1-Sn-50 sample possessed the highest O_{ads} concentration.

H₂-TPR profiles of all of the as-prepared samples are shown in Fig. S13(A), and their H₂ consumption is summarized in Table S5. The Silicalite-1 support exhibited no reduction peaks. When the Sn species were introduced, a weak reduction peak appeared at 472 or 605 °C, which was due to the reduction of the Sn species: Sn⁴⁺ → Sn²⁺ → Sn⁰ [41]. After the addition of Ru, however, the Ru@Silicalite-1 or Ru@Silicalite-1-Sn-50 sample showed a more obvious reduction peak at 140 °C and the reduction of the Sn species was moved toward a lower temperature, which indicates that the Ru-loaded sample was more easily reduced (due to the reduction of the Ru species and surface oxygen species). This result was consistent with the O₂-TPD results (Fig. 5A).

It has been widely accepted that there are two stages in catalytic CVOCs combustion processes: (i) the C–Cl bond is cleaved at the acidic sites; and (ii) the intermediates are deeply oxidized at the redox site [32]. To detect the acidic properties, NH₃-TPD experiments of the

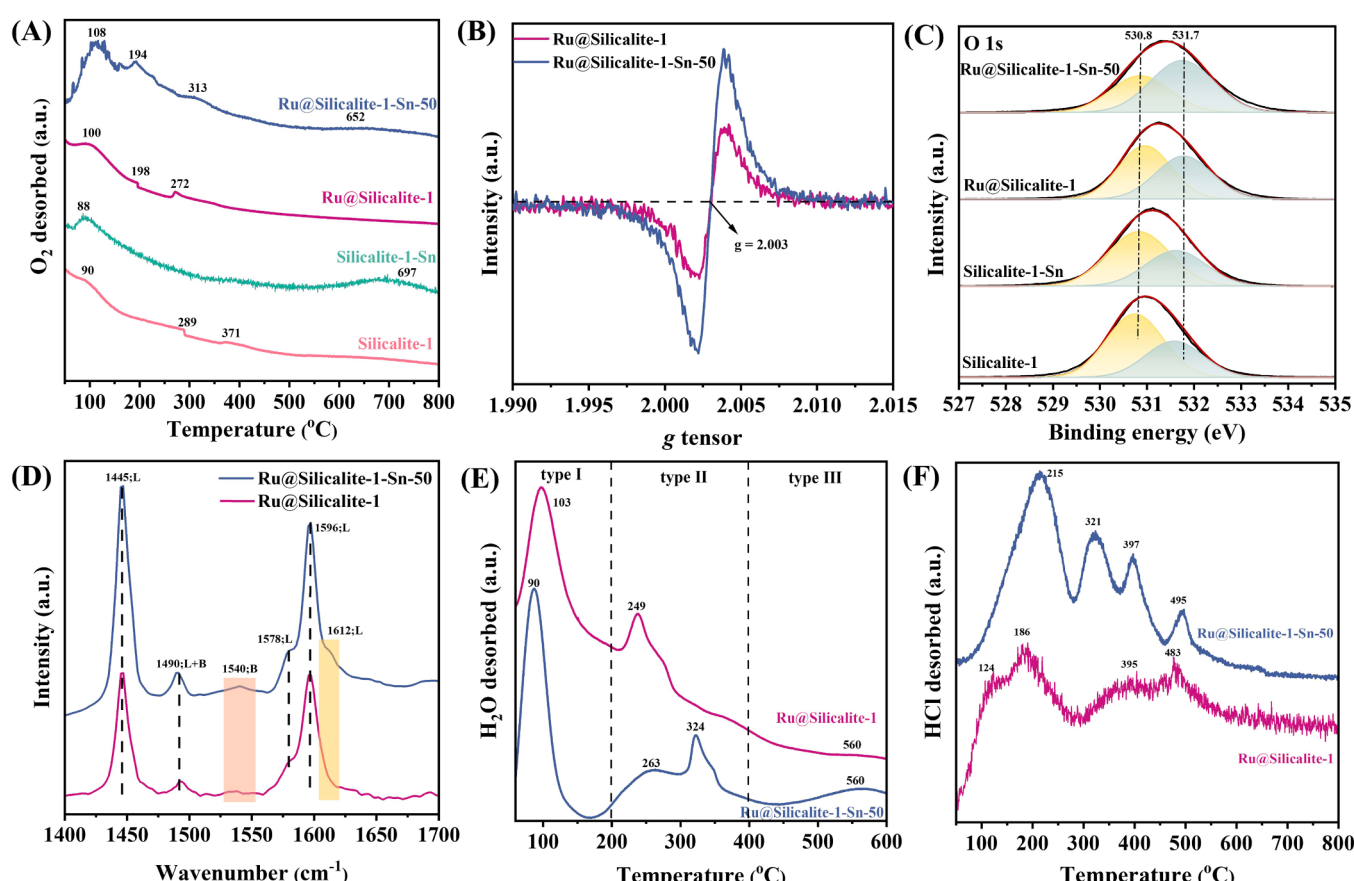


Fig. 5. (A) O₂-TPD profiles, (B) ESR spectra, (C) O 1 s XPS spectra, (D) Py-FTIR spectra after pyridine adsorption at 200 °C, (E) H₂O-TPD profiles, and (F) HCl-TPD profiles of the samples.

samples were carried out, and their profiles are shown in Fig. S13(B). There were mainly two desorption peaks in the ranges of 50–250 and 300–400 °C, which were related to the weak and strong acid sites, respectively. The quantitative desorption results are presented in Table S5. Compared with the Silicalite-1 support, there was a significant increase in the two acid sites of Silicalite-1-Sn after the doping of Sn. However, the introduction of Ru exerted little effect on acidity of the Ru@Silicalite-1 sample.

Acid sites are generally divided into the BAS and LAS, which can be identified using the Py-FTIR technique. As shown in Fig. 5D, the bands at 1445, 1578, 1596, and 1612 cm⁻¹ were attributed to the LAS, while the one at 1540 cm⁻¹ was assigned to the BAS. Besides, the band at 1490 cm⁻¹ was associated with the pyridine adsorbed on both the BAS and LAS [19]. After making a quantitative analysis, the acidity of Ru@Silicalite-1 and Ru@Silicalite-1-Sn-50 is obtained and listed in Table S6. After the doping of Sn, the LAS and BAS amount of Ru@Silicalite-1-Sn-50 significantly increased, which might due to the combination of zeolite confinement and tight coupling between redox sites and acidic sites, with the Ru@Silicalite-1-Sn-50 achieving the higher levels of both weak and strong acid sites. Further exploration on the changing trend of the LAS and BAS strengths of Ru@Silicalite-1 and Ru@Silicalite-1-Sn-50 with temperature was conducted using *in situ* pyridine infrared technique (Fig. S14(A, B)). In the entire temperature range, the LAS and BAS strengths of Ru@Silicalite-1-Sn-50 were higher than those of Ru@Silicalite-1. These abundant acid sites enhanced the adsorption of DCM and strengthened the interaction between reactant and active phase. Besides, more strong acid sites were beneficial for the desorption of the acidic product CO₂ and the cleavage of C–C bonds, which could further accelerate the reaction [42]. The redox property and acidity were the factors influencing catalytic performance of the samples for DCM and toluene combustion. That is to say, both contributed to the improvement in catalytic activity of the samples, in which the redox property was beneficial for O₂ activation and CVOCs deep oxidation, while the acidic sites favored the adsorption of CVOCs. Therefore, the synergistic effect between redox property and acidity was more helpful to improve the catalytic efficiency of CVOCs removal.

To investigate effects of the surface element composition and metal oxidation state on catalytic activity, we used the XPS technique to record Sn 3d, O 1 s, Ru 3d, Ru 3d, and Cl 2p XPS spectra of the fresh and used samples (Fig. S1(A–D)), and their corresponding O_{ads}/O_{latt} and Ru⁰/Ru⁴⁺ molar ratios are summarized in Table S4. XPS spectra of Ru 3d were collected in Fig. S1(A). Ru@Silicalite-1 and Ru@Silicalite-1-Sn showed two peaks at BE = 280.5 and 281.5 eV, attributable to the surface Ru⁰ and Ru⁴⁺ species, respectively. Compared with Ru@Silicalite-1, intensity of the component due to the surface Ru⁰ species became weaker while that due to the surface Ru⁴⁺ species on Ru@Silicalite-1-Sn increased, which indicates the presence of electron transfer between the Ru and Sn species. However, there was little change in amount of the Ru species on the Ru@Silicalite-1-Sn-50 sample after the long-term stability test, indicating that the closely coupled structure of the sample plays an active role in stabilizing the electronic structure of Ru. In addition, there was no significant alteration in surface elemental composition of the Ru@Silicalite-1-Sn-50 sample after the water stability test. Compared with the Ru@Silicalite-1 sample, the Ru⁰/Ru⁴⁺ molar ratio increased from 0.38 to 0.86, indicating a significant decrease of the surface Ru⁴⁺ species that were as an oxidizing agent in the catalytic reactions. Furthermore, there was a deposition of Cl species on the Ru@Silicalite-1 sample surface (Fig. S1(C)), and this sample exhibited a drop in O_{ads} concentration, which might be the main reason for the decrease in stability. The high activity and anti-poisoning of Ru@Silicalite-1-Sn catalyst was due to the presence of a larger amount of acid sites and the facile redox property. Loading of Ru single atom on Silicalite-1-Sn could effectively remove chlorine from the active sites during the Deacon reaction process. In addition, compared with Ru@Silicalite-1, Ru@Silicalite-1-Sn possessed better endurance and Cl-resistance in the oxidation of DCM and toluene. The reason for good tolerance to Cl-poisoning was

that there was a strong interaction between the highly dispersed Ru species and the Silicalite-1-Sn via formation of the Ru–O–Sn-like bond, leading to the enhancement in Cl-resistance of the Ru species to deactivation, after all the Cl species were preferentially adsorbed at the Sn sites and the addition of Sn could protect the active Ru species from Cl-poisoning.

3.4. Chemical adsorption and desorption properties

To evaluate the desorption behaviors of H₂O and HCl, we performed the H₂O-TPD and HCl-TPD experiments of Ru@Silicalite-1 and Ru@Silicalite-1-Sn-50. Fig. 5E shows H₂O-TPD profiles of the two samples, and Table S6 summarizes the contents of three different types of water species. The peak below 200 °C was assigned to the surface physical adsorbed water (Type I), the ones at 200–400 °C were associated with dehydration of the structural hydroxyl group (Type II), and the ones above 400 °C were attributed to the strongly bonded hydroxyl group (Type III) [43]. Previous studies reported that the interaction between Type II water and adsorbed O₂ could generate the *OOH and *OH es [44]. Therefore, the Ru@Silicalite-1-Sn-50 with more amounts of the *OOH and *OH species exhibited better catalytic activity. Moreover, Type II water was the main proton source for the formation of HCl, which could ensure sufficient H⁺ from H₂O and dissociated Cl⁻ reactions, thereby desorbing in the form of HCl. The Cl species captured by oxygen vacancies were unstable and easily reacted with the dissociated H⁺ in H₂O to form HCl, hence promoting desorption of the Cl species [45]. This provides a plausible explanation for the improved conversion of DCM after the water vapor was passed through.

HCl is an important product of DCM oxidation. HCl desorption behaviors of the Ru@Silicalite-1 and Ru@Silicalite-1-Sn-50 samples were investigated, and their results are shown in Fig. 5F. The two samples exhibited similar HCl desorption peaks: The desorption peak below 300 °C was due to the physically adsorbed HCl on the sample surface, while the one above 300 °C belonged to the strongly chemically adsorbed HCl. The desorption amount of Ru@Silicalite-1-Sn-50 was significantly higher than that of Ru@Silicalite-1, which was attributed to the different acidity of the different supports (and hence resulting in significantly different desorption of HCl). The Ru@Silicalite-1-Sn-50 sample was rich in acidic sites, giving rise to the presence of multiple HCl sources on this sample.

The (toluene + DCM)-TPD experiment was performed to verify the enhanced DCM desorption from Ru@Silicalite-1-Sn-50, which might be attributed to the tight coupling between redox and acidic sites. As shown in Fig. 6A, compared with Ru@Silicalite-1, the higher toluene and DCM desorption intensity and lower desorption temperature were observed over the Ru@Silicalite-1-Sn-50 sample, indicating that the interaction between toluene and DCM with Ru@Silicalite-1 was stronger than that with Ru@Silicalite-1-Sn-50. The quantitative analysis data are summarized in Table S5. As one of the important products of DCM oxidation, its HCl desorption signals are shown in Fig. 6B. The Cl atoms in DCM underwent the oxidative dissociation at the acidic sites, the generated Cl atoms combined with protons on the sample to form HCl at low temperatures, and the desorption amount of HCl on Ru@Silicalite-1-Sn-50 was significantly more than that on Ru@Silicalite-1, which was consistent with the H₂O-TPD results. CO₂ and H₂O are the target products of VOCs oxidation. Fig. 6C and D show the desorption peaks of CO₂ and H₂O. Compared with the Ru@Silicalite-1 sample, CO₂ and H₂O desorption amounts of the Ru@Silicalite-1-Sn-50 sample were higher and their desorption peaks were shifted toward lower temperatures, which was related to its higher LAS content.

3.5. Effect of Sn doping on the product distribution

TPSR-MS profiles of mixed VOCs (1000 ppm toluene + 500 ppm DCM + 20 vol% O₂ + N₂ (balance)) oxidation over Ru@Silicalite-1 and Ru@Silicalite-1-Sn-50 were measured, and the main intermediate

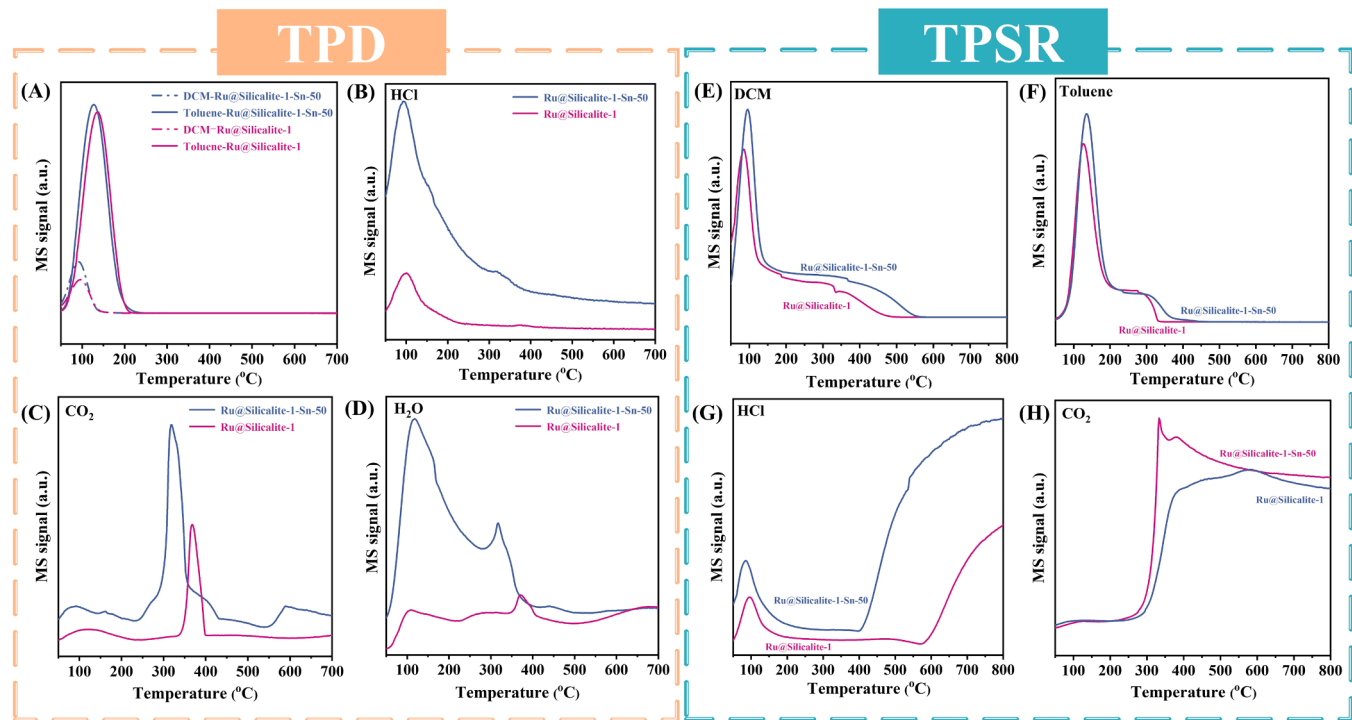


Fig. 6. (A–D) (DCM + toluene)-TPD profiles and (E–H) (DCM + toluene)-TPSR profiles of the Ru@Silicalite-1-Sn-50 and Ru@Silicalite-1 samples.

products were HCl, CO₂, Cl₂, CCl₄, CHCl₃, and CB. As shown in Fig. 6E and F, compared with the Ru@Silicalite-1 sample, the Ru@Silicalite-1-Sn-50 sample displayed stronger DCM and toluene desorption peaks. Stronger DCM adsorption of Ru@Silicalite-1-Sn-50 might be due to the fact that after the doping of Sn, Ru@Silicalite-1-Sn-50 possessed richer acidic sites and thus larger toluene and DCM adsorption capacities, which was in good agreement with the (toluene + DCM)-TPD results. During the oxidation process, the desorption peak intensity of HCl, CO₂, and H₂O from Ru@Silicalite-1-Sn-50 was higher than that from Ru@Silicalite-1, and the desorption amount of HCl was particularly significant (Fig. 6G, F, and S15(A)). As shown in Fig. S15(B), both samples exhibited a desorption peak of Cl₂ at low temperatures (< 100 °C). When the temperature rose to 400 °C, the desorption amount of Cl₂ began to increase, and the Cl₂ desorption amount of the Ru@Silicalite-1 sample was significantly higher than that of the Ru@Silicalite-1-Sn-50 sample. There was the occurrence of the Deacon reaction (HCl + O₂ → Cl₂ + H₂O). However, the mixed VOCs were completely oxidized over Ru@Silicalite-1-Sn-50 at 400 °C, so the Cl₂ generated at high temperatures could be ignored. As shown in Fig. S15(C and D), the desorption peak intensity of the by-products (CCl₄, CHCl₃, and CB) over Ru@Silicalite-1-Sn-50 was significantly lower than that over Ru@Silicalite-1. This result might be due to the fact that the BAS in the Ru@Silicalite-1-Sn-50 sample can provide a more amount of H protons to react with Cl during the reaction process. In addition, the H₂O generated during the reaction could also be dissociated into –OH and H protons at basic sites or oxygen vacancies, thereby improving the selectivity of HCl. Compared with the Ru@Silicalite-1 sample, the Ru@Silicalite-1-Sn-50 sample possessed close coupling between redox sites and acidic centers, which exhibited better catalytic performance and anti-deactivation performance.

In order to further investigate the influence of doped Sn species on the formation of organic by-products, the products of mixed VOCs (toluene + DCM) oxidation at different temperatures are shown in Fig. 7A and B and S16. In addition to the reactants (toluene and DCM), eight intermediate products (C₇H₇Cl, C₇H₆O, C₆H₇Cl, C₆H₅Cl, CHCl₃, C₆H₆, CCl₄, and CH₃Cl) were detected (Fig. 7A). When the temperature rose, the number of the intermediate by-products gradually decreased,

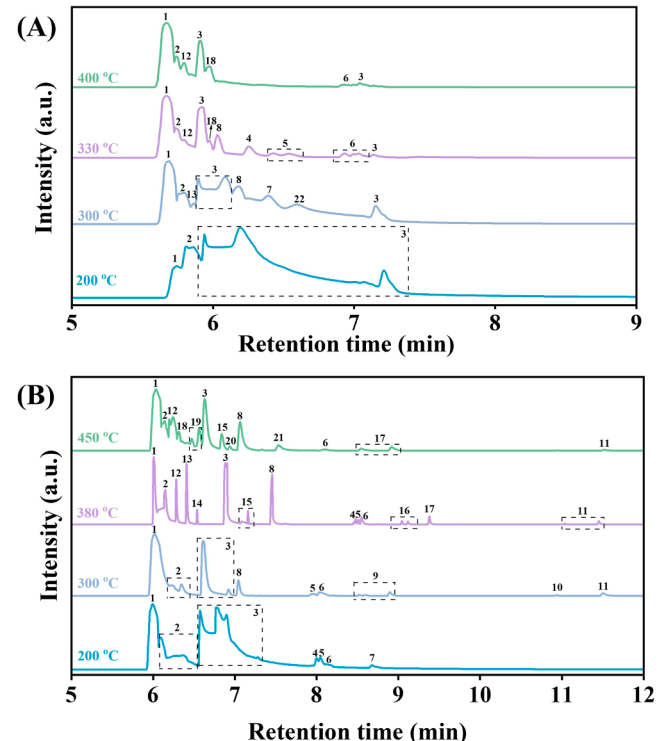


Fig. 7. Reaction intermediates detected during the mixed VOCs oxidation process over (A) Ru@Silicalite-1-Sn-50 and (B) Ru@Silicalite-1 at different temperatures.

and only CHCl₃, CCl₄, and C₇H₆O were detected in the end. Compared with the Ru@Silicalite-1-Sn-50 sample, however, the number of the toxic substances produced over the Ru@Silicalite-1 sample during the reaction process increased sharply (to 17 kinds of toxic substances), as shown in Fig. S16. To further verify the positive effect of close coupling

between redox and acidic sites in the Ru@Silicalite-1-Sn-50 sample, we also made a analysis on the products formed over the Ru/SnO₂/Silicalite-1 sample. As shown in Fig. S17, there were 13 products detected during the reaction process, and 8 by-products were still detected after the complete oxidation of mixed VOCs. Based on the TPSR results, we consider that the tightly coupled active sites formed in the Ru@Silicalite-1-Sn-50 sample not only improve the selectivities of CO₂ and HCl, but also greatly reduce the generation of chlorine-containing by-products.

3.6. Possible mechanism of mixed VOCs oxidation over Ru@Silicalite-1-Sn-50

The in situ DRIFTS technique was used to investigate the adsorption and reaction mechanism of mixed VOCs over the samples. As shown in Fig. 8A, in situ DRIFTS spectra of the Ru@Silicalite-1-Sn-50 sample after adsorption of (1000 ppm toluene + 500 ppm DCM + 20 vol% O₂ + N₂ (balance)) at 50 °C for different time. The bands at 705 and 743 cm⁻¹ were related to the gaseous chemical adsorption of DCM, the one at 810 cm⁻¹ was assigned to the stretching vibration of the C–Cl bonds in DCM, the ones at 1270, 2983, and 3067 cm⁻¹ could be assigned to the symmetric and anti-symmetric stretching vibrations of DCM [33], and the ones at 1370 and 1420 cm⁻¹ were due to the stretching vibration of the CHCl₂ group in DCM [46]. The absorption band at 1507 cm⁻¹ was owing to the planar skeleton vibration of the benzene ring. The characteristic absorption band at 2926 cm⁻¹ was attributed to the stretching

vibration of the C–H bonds in aromatic ring, and the one at 3038 cm⁻¹ was ascribed to the asymmetric stretching vibration of methyl C–H bonds in toluene [47]. The band at 1601 cm⁻¹ was the hydroxyl (–OH) vibration signal of water adsorbed on the sample surface. However, there were two negative bands at 3691 cm⁻¹ (bridged type –OH: it provided adsorption sites for chlorine-containing species) and 3742 cm⁻¹ (end type –OH) [48], which were consumed during the adsorption processes. As the adsorption time extended, the characteristic absorption bands due to toluene and DCM gradually increased in intensity.

As shown in Fig. 8B, in situ mixed VOCs oxidation was carried out over the Ru@Silicalite-1-Sn-50 sample at different temperatures (50–450 °C). When the temperature rose, intensity of the characteristic absorption bands of DCM and toluene gradually decreased and finally disappeared, and new bands appeared at the same time some. The absorption band at 1120 cm⁻¹ was assigned to the stretching vibration of O–CH₂Cl, which was formed due to the nucleophilic attack by the surface oxygen atoms after the removal of a Cl atom from DCM [49]. The band at 1847 cm⁻¹ was attributed to the vibrational mode of anhydride, the one at 992 cm⁻¹ was the stretching vibration of the C–O bond in methoxide [50], and the ones at 1168 and 1217 cm⁻¹ were symmetric stretching vibrations of the C=O bond in the carboxylic acid group [51]. Intensity of these bands increased with the rise in temperature.

Combining the results of in situ DRIFTS, GC–MS, and TPSR measurements, we think that the reaction pathways of mixed VOCs (toluene + DCM) over Ru@Silicalite-1-Sn-50 are as follows (Scheme 2): (i) DCM

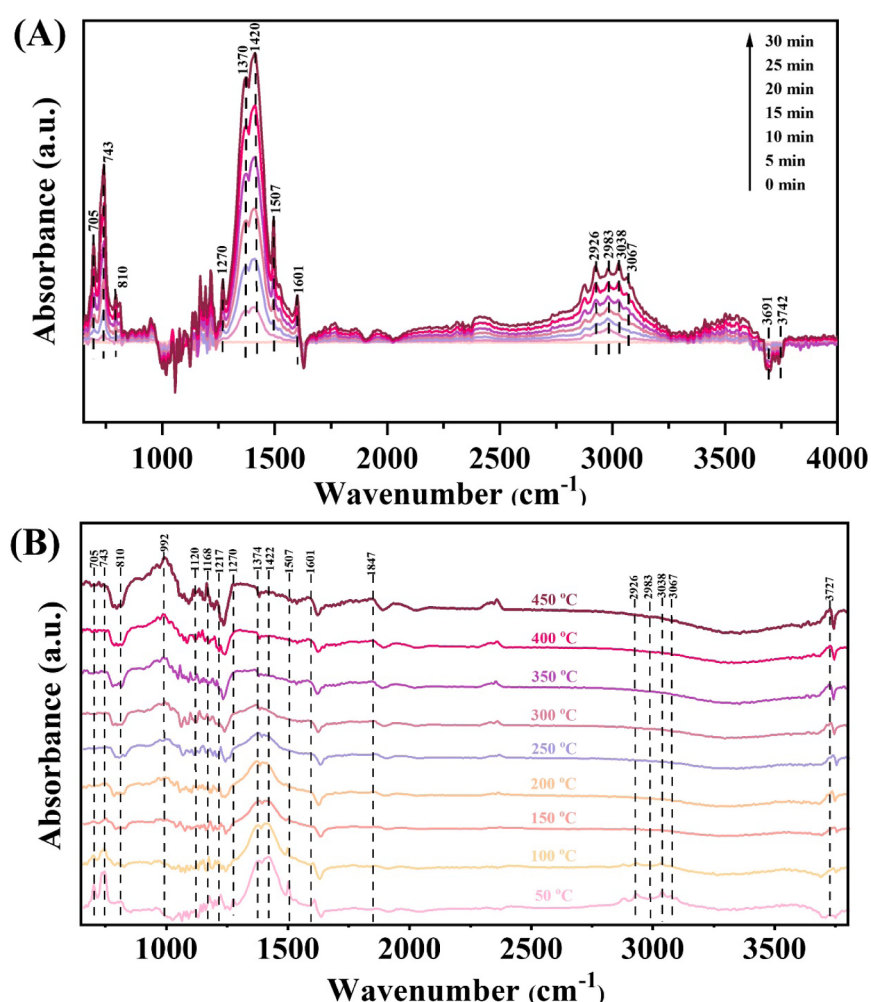
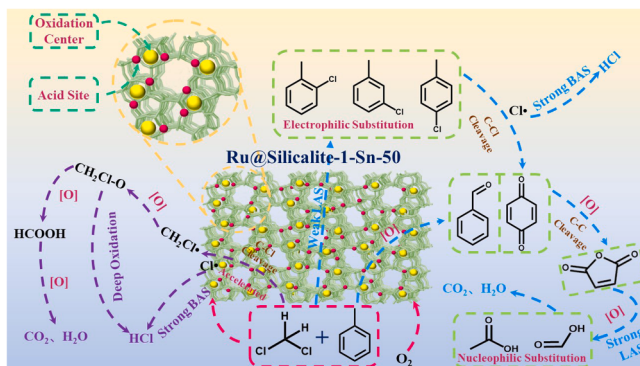


Fig. 8. In situ DRIFTS spectra of mixed VOCs oxidation over the Ru@Silicalite-1-Sn-50 sample in (A) (1000 ppm toluene + 500 ppm DCM + 20 vol% O₂ + N₂ (balance)) at 50 °C for 30 min and (B) (1000 ppm toluene + 500 ppm DCM + 20 vol% O₂ + N₂ (balance)) at 50–450 °C.



Scheme 2. The possible mechanism of mixed VOCs oxidation over the Ru@Silicalite-1-Sn-50 sample.

and toluene molecules are adsorbed at the BAS or O_{vac} on the surface of the sample; (ii) the C–Cl bond cleavage is accelerated and a nucleophilic substitution occurs with the active oxygen species to form CH₂Cl–O; (iii) gas-phase oxygen continues to attack CH₂Cl–O to produce formaldehyde; and (iv) formaldehyde undergoes further deep oxidation at the strong LAS to generate some intermediate products (i.e., formic acid), and are finally oxidized to CO₂, H₂O, and HCl. At the same time, the oxidation of toluene also occurs simultaneously, and toluene is first oxidized to benzoquinone. As the temperature rises, benzoquinone undergoes a cyclic cracking reaction to produce maleic anhydride under the action of oxygen. Maleic anhydride is further deeply converted to acetic acid and formic acid, and finally oxidized to CO₂ and H₂O. The generation of chlorination by-products during the oxidation process cannot be ignored. The production of these chlorination by-products is mainly concentrated at the weak LAS. When the oxygen content in the gas phase is insufficient, the dissociated Cl species undergoes an electrophilic substitution with toluene, generating monochlorotoluene, dichlorobenzene, and etc. A series of oxidation reactions of these intermediates take place to eventually produce CO₂, H₂O, and HCl. In contrast, the Ru@Silicalite-1 sample lacks acidic sites and oxygen vacancies, thus limiting DCM adsorption and C–Cl bond cleavage. Overall, by optimizing the synergistic action between the redox and acidic sites, the deep oxidation of intermediates can be promoted and the generation of chlorinated by-products can be significantly suppressed.

4. Conclusions

The Ru@Silicalite-1-Sn-x samples were prepared using a hydrothermal method. The doping of Sn to Silicalite-1 could enrich the BAS and LAS, thus enhancing the adsorption of CVOCs molecules. In addition, the introduction of Sn could also increase the dispersion of Ru and oxygen vacancies, which led to the formation of tightly coupled redox and acidic sites on the sample. In the mixed VOCs (DCM + toluene) oxidation system, less chlorinated by-products were formed over the Ru@Silicalite-1-Sn-50 sample. The acidic sites were effective in the dissociation of C–Cl bonds in CVOCs, and the intermediate products were oxidized to CO₂, H₂O, and HCl at the redox sites in contact with the nearby acidic sites. The Ru@Silicalite-1-Sn-50 sample showed the best catalytic performance in mixed VOCs oxidation ($T_{90\%(\text{Toluene})} = 287^\circ\text{C}$ and $T_{90\%(\text{DCM})} = 361^\circ\text{C}$ at SV = 40,000 mL/(g h); specific reaction rate and TOF_{Ru} for toluene oxidation at 170 °C were 9.67 μmol/(g_{cat} h) and $0.98 \times 10^{-3}\text{ s}^{-1}$, and specific reaction rate and TOF_{Ru} for DCM oxidation at 200 °C were 3.84 μmol/(g_{cat} h) and $0.46 \times 10^{-3}\text{ s}^{-1}$, respectively). At the same time, the Ru@Silicalite-1-Sn-50 sample exhibited long-term stability (within 100 h of (DCM + toluene) oxidation at 380 °C) and good water resistance in the oxidation of mixed VOCs. The present work demonstrates the construction of effective catalysts with balanced redox and acidity properties, which can provide a simple strategy for rationally designing full-featured catalysts suitable for the oxidation of VOCs and

CVOCs under the practical conditions.

CRediT authorship contribution statement

Linke Wu: Investigation. **Xiaohui Yu:** Investigation. **Lin Jing:** Software. **Yuxi Liu:** Writing – review & editing. **Jiguang Deng:** Writing – review & editing. **Hongxing Dai:** Writing – review & editing, Project administration. **Ying Feng:** Software. **Ruyi Gao:** Investigation. **Jinxiong Tao:** Investigation.

Declaration of Competing Interest

The authors declare that they have no known competing financial interests or personal relationships that could have appeared to influence the work reported in this paper.

Data availability

No data was used for the research described in the article.

Acknowledgements

This work was supported by the National Key R&D Program of China (2022YFB3504101 and 2022YFB3506200), National Natural Science Committee of China–Liaoning Provincial People's Government Joint Fund (U1908204x), National Natural Science Foundation of China (21976009 and 2196116074), Foundation on the Creative Research Team Construction Promotion Project of Beijing Municipal Institutions (IDHT20190503), Beijing Natural Science Foundation (J210006x), R&D Program of Beijing Municipal Education Commission (KZ202210005011), and Development Program for the Youth Outstanding–Notch Talent of Beijing Municipal Commission of Education (CIT&TCD201904019).

Appendix A. Supporting information

Supplementary data associated with this article can be found in the online version at doi:10.1016/j.apcatb.2024.123910.

References

- [1] F. Lin, X. Li, Z. Zhang, N. Li, B. Yan, C. He, Z. Hao, G. Chen, Comprehensive review on catalytic degradation of Cl-VOCs under the practical application conditions, *Crit. Rev. Environ. Sci. Technol.* 52 (2020) 311–355.
- [2] W. Zhan, Y. Guo, X. Gong, Y. Guo, Y. Wang, G. Lu, Current status and perspectives of rare earth catalytic materials and catalysis, *Chin. J. Catal.* 35 (2014) 1238–1250.
- [3] B. Huang, C. Lei, C. Wei, G. Zeng, Chlorinated volatile organic compounds (Cl-VOCs) in environment – sources, potential human health impacts, and current remediation technologies, *Environ. Inter.* 71 (2014) 118–138.
- [4] C. He, J. Cheng, X. Zhang, M. Douthwaite, S. Pattisson, Z. Hao, Recent advances in the catalytic oxidation of volatile organic compounds: A review based on pollutant sorts and sources, *Chem. Rev.* 119 (2019) 4471–4568.
- [5] Q. Dai, W. Wang, X. Wang, G. Lu, Sandwich-structured CeO₂@ZSM-5 hybrid composites for catalytic oxidation of 1,2-dichloroethane: an integrated solution to coking and chlorine poisoning deactivation, *Appl. Catal. B* 203 (2017) 31–42.
- [6] H. Liu, J. Yang, Y. Jia, Z. Wang, M. Jiang, K. Shen, H. Zhao, Y. Guo, Y. Guo, L. Wang, S. Dai, W. Zhan, Significant improvement of catalytic performance for chlorinated volatile organic compound oxidation over RuO_x supported on acid-etched Co₃O₄, *Environ. Sci. Technol.* 55 (2021) 10734–10743.
- [7] X. Weng, Q. Meng, J. Liu, W. Jiang, S. Pattisson, Z. Wu, Catalytic oxidation of chlorinated organics over lanthanide perovskites: effects of phosphoric acid etching and water vapor on chlorine desorption behavior, *Environ. Sci. Technol.* 53 (2019) 884–893.
- [8] Y. Sun, S. Xu, B. Bai, L. Li, Y. Kang, X. Hu, Z. Liao, C. He, Biotemplate fabrication of hollow tubular Ce_xSr_{1-x}TiO₃ with regulable surface acidity and oxygen mobility for efficient destruction of chlorobenzene: intrinsic synergy effect and reaction mechanism, *Environ. Sci. Technol.* 56 (2022) 5796–5807.
- [9] Y. Wang, G. Wang, W. Deng, J. Han, L. Qin, B. Zhao, L. Guo, F. Xing, Study on the structure-activity relationship of Fe–Mn oxide catalysts for chlorobenzene catalytic combustion, *Chem. Eng. J.* 395 (2020) 1385–8947.
- [10] X. Yu, J. Deng, Y. Liu, L. Jing, R. Gao, Z. Hou, Z. Zhang, H. Dai, Enhanced water resistance and catalytic performance of Ru/TiO₂ by regulating Brønsted acid and

- oxygen vacancy for the oxidative removal of 1,2-dichloroethane and toluene, Environ. Sci. Technol. 56 (2022) 11739–11749.
- [11] Y. Su, K. Fu, C. Pang, Y. Zheng, C. S. N. Ji, D. Ma, X. Lu, C. Liu, R. Han, Q. Liu, Recent advances of chlorinated volatile organic compounds' oxidation catalyzed by multiple catalysts: reasonable adjustment of acidity and redox properties, Environ. Sci. Technol. 56 (2022) 9854–9871.
- [12] P. Yang, S. Zuo, R. Zhou, Synergistic catalytic effect of $(Ce,Cr)_xO_2$ and HZSM-5 for elimination of chlorinated organic pollutants, Chem. Eng. J. 323 (2017) 160–170.
- [13] H. Wang, B. Peng, R. Zhang, H. Chen, Y. Wei, Synergies of Mn oxidative ability and ZSM-5 acidity for 1,2-dichloroethane catalytic elimination, Appl. Catal. B 276 (2020) 118922.
- [14] P. Sun, W. Wang, X. Dai, X. Weng, Z. Wu, Mechanism study on catalytic oxidation of chlorobenzene over $Mn_xCe_{1-x}O_2/H$ -ZSM5 catalysts under dry and humid conditions, Appl. Catal. B 198 (2016) 389–397.
- [15] M. Romero-Sáez, D. Divakar, A. Aranzabal, J.R. González-Velasco, J.A. González-Marcos, Catalytic oxidation of trichloroethylene over Fe-ZSM-5: influence of the preparation method on the iron species and the catalytic behavior, Appl. Catal. B 180 (2016) 210–218.
- [16] Z. Li, R. Gao, Z. Hou, X. Yu, H. Dai, J. Deng, Y. Liu, Tandem supported Pt and ZSM-5 catalyst with separated catalytic functions for promoting multicomponent VOCs oxidation, Appl. Catal. B 339 (2023) 123131.
- [17] J. Shi, Y. Wang, W. Yang, Z. Xie, Recent advances of pore system construction in zeolite-catalyzed chemical industry processes, Chem. Soc. Rev. 44 (2015) 8877–8903.
- [18] E. Yuan, W. Dai, G. Wu, N. Guan, M. Hunger, L. Li, Facile synthesis of Sn-containing MFI zeolites as versatile solid acid catalysts, Microporous Mesoporous Mater. 270 (2018) 265–273.
- [19] J. Zhao, W. Xi, C. Tu, Q. Dai, X. Wang, Catalytic oxidation of chlorinated VOCs over Ru/Ti_xSn_{1-x} catalysts, Appl. Catal. B 263 (2020) 118237.
- [20] C. Xia, Y. Liu, M. Lin, X. Peng, B. Zhu, X. Shu, Confirmation of the isomorphous substitution by Sn atoms in the framework positions of MFI-typed zeolite, Catal. Today 316 (2018) 193–198.
- [21] N.K. Mal, A.V. Ramaswamy, Hydroxylation of phenol over Sn-silicalite-1 molecular sieve: solvent effects, J. Mol. Catal. A 105 (1996) 149–158.
- [22] K. Chaudhari, T.K. Das, P.R. Rajamohan, K. Lazar, S. Sivasanker, A. J. Chandwadkar, Synthesis, characterization, and catalytic properties of mesoporous tin-containing analogs of MCM-41, J. Catal. 183 (1999) 281–291.
- [23] Y. Feng, W. Li, M. Meng, H. Yin, J. Mi, Mesoporous Sn(IV) doping MCM-41 supported Pd nanoparticles for enhanced selective catalytic oxidation of 1,2-propanediol to pyruvic acid, Appl. Catal. B 253 (2019) 111–120.
- [24] C. Hammond, S. Conrad, I. Hermans, Simple and scalable preparation of highly active Lewis acid Sn- β , Angew. Chem. Int. Ed. 51 (2012) 11736–11739.
- [25] P.Y. Dapsens, C. Mondelli, J.P. Ramírez, Design of Lewis-acid centres in zeolitic matrices for the conversion of renewables, Chem. Soc. Rev. 44 (2015) 7025–7043.
- [26] N.K. Mal, V. Ramaswamy, P.R. Rajamohan, A.V. Ramaswamy, Sn-MFI molecular sieves: synthesis methods, ²⁹Si liquid and solid MAS NMR, ¹¹⁹Sn static and MAS NMR studies, Microporous Mater. 12 (1997) 331–340.
- [27] J. Qiu, J. Hu, J. Lan, L. Wang, G. Fu, R. Xiao, B. Ge, J. Jiang, Pure Siliceous zeolite-supported Ru single-atom sites for ammonia synthesis, Chem. Mater. 31 (2019) 9413–9421.
- [28] L. Kang, B. Wang, A. Thetford, K. Wu, M. Danaie, Q. He, E. Gibson, L. Sun, H. Asakura, C. Catlow, F. Wang, Design, identification, and evolution of a surface ruthenium (II/III) single site for CO activation, Angew. Chem. Int. Ed. 60 (2021) 1212–1219.
- [29] L. Wang, M. Sakurai, H. Kameyama, Catalytic oxidation of dichloromethane and toluene over platinum alumite catalyst, J. Hazard. Mater. 154 (2008) 390–395.
- [30] H. Deng, Y. Lu, T. Pan, L. Wang, C. Zhang, H. He, Metals incorporated into OMS-2 lattice create flexible catalysts with highly efficient activity in VOCs combustion, Appl. Catal. B 320 (2023) 121955.
- [31] X. Fei, W. Ouyang, Z. Gu, S. Cao, H. Wang, X. Weng, Z. Wu, Effect of Cr doping in promoting the catalytic oxidation of dichloromethane (CH_2Cl_2) over Cr-Co@Z catalysts, J. Hazard. Mater. 413 (2021) 125327.
- [32] Y. Su, K. Fu, Y. Zheng, N. Ji, C. Song, D. Ma, X. Lu, R. Han, Q. Liu, Catalytic oxidation of dichloromethane over Pt–Co/HZSM-5 catalyst: synergistic effect of single-atom Pt, Co_3O_4 , and HZSM-5, Appl. Catal. B 288 (2021) 119980.
- [33] Y. Wang, P. Wang, X. Lu, N. Hu, Q. Wang, S. Wu, W. Deng, L. Wang, Construction of mesoporous Ru@ZSM-5 catalyst for dichloromethane degradation: synergy between acidic sites and redox centres, Fuel 346 (2023) 128337.
- [34] F. Zhou, Q. Xin, Y. Fu, Z. Hua, Y. Dong, M. Ran, H. Song, S. Liu, R. Qu, Y. Yang, X. Zhang, C. Zheng, X. Gao, Efficient catalytic oxidation of chlorinated volatile organic compounds over RuO_2 – WO_3 /Sn_{0.2}Ti_{0.8}O₂ catalysts: Insight into the Cl poisoning mechanism of acid sites, Chem. Eng. J. 464 (2023) 142471.
- [35] Q. Dai, Z. Zhang, J. Yan, J. Wu, G. Johnson, W. Sun, X. Wang, S. Zhang, W. Zhan, Phosphate-functionalized CeO₂ nanosheets for efficient catalytic oxidation of dichloromethane, Environ. Sci. Technol. 52 (2018) 13430–13437.
- [36] Q. Chen, N. Li, M. Luo, J. Lu, Catalytic oxidation of dichloromethane over Pt/CeO₂–Al₂O₃ catalysts, Appl. Catal. B 127 (2012) 159–166.
- [37] X. Liu, L. Chen, T. Zhu, R. Ning, Catalytic oxidation of chlorobenzene over noble metals (Pd, Pt, Ru, Rh) and the distributions of polychlorinated by-products, J. Hazard. Mater. 363 (2019) 90–98.
- [38] J. An, Y. Wang, J. Lu, J. Zhang, Z. Zhang, S. Xu, X. Liu, T. Zhang, M. Gocyla, M. Heggen, R.E. Dunin-Borkowski, P. Fornasiero, F. Wang, Acid-promoter-free ethylene methoxycarbonylation over Ru-clusters/ceria: the catalysis of interfacial Lewis acid-base pair, J. Am. Chem. Soc. 140 (2018) 4172–4181.
- [39] H. Huang, Y. Gu, J. Zhao, X. Wang, Catalytic combustion of chlorobenzene over VO_x/CeO₂ catalysts, J. Catal. 326 (2015) 54–68.
- [40] Y. Feng, W. Wang, M. Hua, Y. Liu, L. Jing, L. Wei, Z. Hou, X. Wang, X. Yu, L. Wu, Y. Jiang, J. Deng, H. Dai, Differences between atomically-dispersed and particulate Pt supported catalysts on synergistic photothermocatalytic oxidation of VOCs from cooking oil fumes, Appl. Catal. B 339 (2023) 123116.
- [41] X. Yu, L. Dai, J. Deng, Y. Liu, L. Jing, X. Zhang, X. Jiang, Z. Hou, J. Wang, H. Dai, Catalytic performance and intermediates identification of trichloroethylene deep oxidation over Ru/3DOM SnO₂ catalysts, J. Catal. 400 (2021) 310–324.
- [42] X. Wang, P. Sun, Y. Long, Q. Meng, Z. Wu, Catalytic oxidation of chlorobenzene over $Mn_xCe_{1-x}O_2/H$ -ZSM-5 catalysts: a study with practical implications, Environ. Sci. Technol. 51 (2017) 8057–8066.
- [43] P. Sun, S. Zhai, J. Chen, J. Yuan, Z. Wu, X. Weng, Development of a multi-active center catalyst in mediating the catalytic destruction of chloroaromatic pollutants: a combined experimental and theoretical study, Appl. Catal. B 272 (2020) 119015.
- [44] H. Chen, Y. Liu, R. Gao, T. Dong, Z. Hou, L. Jing, E. Duan, J. Deng, H. Dai, N-doped carbon-modified palladium catalysts with superior water resistant performance for the oxidative removal of toxic aromatics, J. Hazard. Mater. 437 (2022) 129358.
- [45] H.A. Miran, M. Altarawneh, Z. Jiang, H. Osikierski, M. Almatarnehc, B. Z. Drlugorska, Decomposition of selected chlorinated volatile organic compounds by ceria (CeO₂), Catal. Sci. Technol. 7 (2017) 3902–3919.
- [46] S. Xu, Y. Ma, K. Zhang, A. Jia, J. Chen, Me Luo, Y. Wang, J. Lu, Catalytic oxidation of dichloromethane over phosphate-modified Co₃O₄: improved performance and control of byproduct selectivity by Co₃O₄ defects and surface acidity, Appl. Surf. Sci. 606 (2022) 154924.
- [47] S. Huang, C. Zhang, H. He, Complete oxidation of o-xylene over Pd/Al₂O₃ catalyst at low temperature, Catal. Today 139 (2008) 15–23.
- [48] S. Xie, Z. Shen, J. Deng, P. Guo, Q. Zhang, H. Zhang, C. Ma, Z. Jiang, J. Cheng, D. Deng, Y. Wang, Visible light-driven C–H activation and C–C coupling of methanol into ethylene glycol, Nat. Commun. 9 (2018) 1181.
- [49] L. Zhang, W. Deng, Y. Cai, Q. Dai, L. Guo, Comparative studies of phosphate-modified CeO₂ and Al₂O₃ for mechanistic understanding of dichloromethane oxidation and chloromethane formation, ACS Catal. 10 (2020) 13109–13124.
- [50] C. Binet, M. Daturi, Methanol as an IR probe to study the reduction process in ceria-zirconia mixed compounds, Catal. Today 70 (2001) 155–167.
- [51] G.Ya Popova, T.V. Andrushkevich, Yu.A. Chesalov, E.S. Stoyanov, In situ FTIR study of the adsorption of formaldehyde, formic acid, and methyl formate at the surface of TiO₂ (anatase), Kinet. Catal. 41 (2000) 805–811.